Journal of the Mechanics and Physics of Solids 103 (2017) 22–39

Contents lists available at ScienceDirect

Journal of the Mechanics and Physics of Solids

journal homepage: www.elsevier.com/locate/jmps

A multiscale crack-bridging model of cellulose nanopaper

Qinghua Meng[a], Bo Li[a], Teng Li[b,*], Xi-Qiao Feng[a,*]

[a] Institute of Biomechanics and Medical Engineering, AML, Department of Engineering Mechanics, Tsinghua University, Beijing 100084, China

[b] Department of Mechanical Engineering, University of Maryland, College Park, Maryland 20742, USA

ARTICLE INFO

Article history:
Received 22 January 2017
Revised 2 March 2017
Accepted 7 March 2017
Available online 9 March 2017

Keywords:
Cellulose nanopaper
Fracture toughness
Crack-bridging model
Cohesive law
Hydrogen bond

ABSTRACT

The conflict between strength and toughness is a long-standing challenge in advanced materials design. Recently, a fundamental bottom-up material design strategy has been demonstrated using cellulose nanopaper to achieve significant simultaneous increase in both strength and toughness. Fertile opportunities of such a design strategy aside, mechanistic understanding is much needed to thoroughly explore its full potential. To this end, here we establish a multiscale crack-bridging model to reveal the toughening mechanisms in cellulose nanopaper. A cohesive law is developed to characterize the interfacial properties between cellulose nanofibrils by considering their hydrogen bonding nature. In the crack-bridging zone, the hydrogen bonds between neighboring cellulose nanofibrils may break and reform at the molecular scale, rendering a superior toughness at the macroscopic scale. It is found that cellulose nanofibrils exhibit a distinct size-dependence in enhancing the fracture toughness of cellulose nanopaper. An optimal range of the length-to-radius ratio of nanofibrils is required to achieve higher fracture toughness of cellulose nanopaper. A unified law is proposed to correlate the fracture toughness of cellulose nanopaper with its microstructure and material parameters. The results obtained from this model agree well with relevant experiments. This work not only helps decipher the fundamental mechanisms underlying the remarkable mechanical properties of cellulose nanopaper but also provides a guide to design a wide range of advanced functional materials.

1. Introduction

Many engineering structures require materials with both high strength and high toughness, but these two mechanical properties are usually mutually exclusive. Overcoming the conflict between high strength and high toughness is a long-standing challenge in advanced materials design (Gao et al., 2003; Ji and Gao, 2004; Fu et al., 2008; Ritchie, 2011), and there only exists limited success to address this challenge. Such existing efforts often involve material-specific and complicated synthesis processes (e.g., growing high density nanotwins in metals (Jang et al., 2012; Wei et al., 2014) and bulk metallic glass with isolated dendrites (Hoffman et al., 2008)) and thus are not readily applicable to other materials. A general material design strategy to address the conflict between strength and toughness still remains elusive. Recently, it has been demonstrated that both the strength and toughness of cellulose nanopaper can be enhanced significantly by decreasing the diameter of the constituent cellulose nanofibrils (Henriksson et al., 2008; Zhu et al., 2015). The fundamental bottom-up material design strategy underpinning the strong and tough cellulose nanopaper (Zhu et al., 2015) is shown to be applicable

* Corresponding authors.
E-mail addresses: lit@umd.edu (T. Li), fengxq@tsinghua.edu.cn (X.-Q. Feng).

http://dx.doi.org/10.1016/j.jmps.2017.03.004
0022-5096/

to other material systems, e.g., high performance carbon fibers (Li et al., 2015). Further exploration of the rich potential of such a general material design strategy requires fundamental understanding of the deformation and failure mechanisms of cellulose nanopaper. For example, deciphering the dependence of the mechanical properties of cellulose nanopaper on their constituent building blocks and microstructure is of particular significance for optimizing the performance of other related advanced engineering nanomaterials. To this end, we here establish a multiscale theoretical model to quantitatively study such dependence.

Cellulose nanopaper is a transparent film made of network-forming cellulose nanofibrils. Henriksson et al. (2008) showed that the plastic yield of cellulose nanopaper is associated with the debonding and slippage of cellulose nanofibrils. Under a high shear stress, the interfacial hydrogen bonds between neighboring cellulose nanofibrils may break and reform, and new nanofibril positions are then locked in. This deformation mechanism of cellulose nanopaper was confirmed by Zhu et al. (2015) through atomistic simulations. González et al. (2014) found that cellulose nanopaper has much better mechanical properties than regular paper due to the strong adhesion between cellulose nanofibrils and the high intrinsic mechanical properties of nanocellulose. Zhu et al. (2015) demonstrated that the strength and toughness of cellulose nanopaper are even higher than those of carbon nanotube films.

The crack-bridging model (Bao and Suo, 1992) has been widely used to investigate the fracture problems of fiber-reinforced composites. This model can evaluate the effects of fiber distribution, bridging size, and interfacial parameters on the fracture toughness of composites (Budiansky and Amazigo, 1989; Rubinstein and Xu, 1992; Bao and Song, 1993; Meda and Steif, 1994; Liu et al., 1998). For example, Sun and Jin (2006) examined, by combining a crack-bridging zone and a cohesive zone, the fracture toughness of composites with the fiber-bridging effect. Lin and Li (1997) considered the slip-hardening interface for discontinuous, fiber-reinforced cement-based composites and predicted the enhanced toughness in terms of the ultimate tensile strain and fracture energy of composites. Bertoldi et al. (2007) calculated the stress intensity factor of a crack reinforced by discrete-bridging fibers. Chen et al. (2011) studied the toughness of nanocomposites reinforced by curved nanotubes. They described the toughness by using a function of the curvature, strength, and interfacial friction resistance of nanotubes. Recently, Shao et al. (2012, 2014a, 2014b) investigated the bridging toughening mechanism of platelets in nacre and revealed a significant size effect of platelets on the fracture toughness of nacre. These efforts have deepened our understanding of the toughening mechanisms of fiber-reinforced composites.

It has been revealed that the interfacial hydrogen bonds between nanofibrils play a pivotal role in the toughening of cellulose nanopaper (Henriksson et al., 2008; Zhu et al., 2015). A quantitative correlation between the inter-molecular hydrogen bonds and the inter-nanofibril adhesion properties is crucial for studying the mechanical properties of cellulose nanopaper. Due to a lack of elaborate consideration on interfacial interaction at microscale, the crack-bridging models proposed previously for composites cannot be employed directly to analyze the mechanical properties of cellulose nanopaper. In this paper, therefore, a multiscale theoretical model that correlates the fracture with microstructure is established to investigate the toughening mechanisms in cellulose nanopaper. A cohesive law accounting for the inter-molecular chain hydrogen bonds at the molecular scale is first developed to characterize the repeated breaking and reforming of interfacial hydrogen bonds in the pullout process of neighboring cellulose nanofibrils. It is found that the fracture toughness of cellulose nanopaper shows a distinct dependence on the sizes of cellulose nanofibrils, which should be in an optimal range in order to achieve a higher fracture toughness of cellulose nanopaper. A unified law is given to correlate the toughness of cellulose nanopaper with its microstructure and material parameters. The present model finds agreement with relevant experiments.

2. Cohesive law of cellulose nanofibril interfaces

We first develop a cohesive law for the interfaces between neighboring cellulose nanofibrils by considering their inter-molecular chain hydrogen binding features. Cellulose is a linear chain of ringed glucose molecules with identical units, each of which comprises two anhydroglucose rings ($C_6H_{10}O_5$) linked by $C-O-C$ covalent bonds, as shown in Fig. 1(a) (Moon et al., 2011). Native cellulose exists in two different crystal forms, i.e., I_α and I_β (Atalla and Vanderhart, 1984). Cellulose molecular chains are assembled by intrachain hydrogen bonds into sheets that stack on top of each other to generate crystalline nanofibrils (5 – 50 nm in diameter) (Jarvis, 2003). The interchain hydrogen bonds between neighboring cellulose molecules are primarily of the strong $O6-H\cdots O3$ type (Qian et al., 2005). The superior mechanical properties of cellulose nanopaper are attributed to the high adhesion between nanofibrils endowed by interchain hydrogen bonds (González et al., 2014; Zhu et al., 2015). The molecular structure and hydrogen bonds of neighboring cellulose molecular chains are shown in Fig. 1(b) (Nishiyama et al., 2002; Parthasarathi et al., 2011).

For a hydrogen bond $D-H\cdots A$, the elements D and A are referred to as a hydrogen donor and a hydrogen acceptor, respectively, as shown in Fig. 1(c). The potential energy of a hydrogen bond can be expressed as (Mayo et al., 1990)

$$U(r)=U_0\left[5\left(\frac{s}{r}\right)^{12}-6\left(\frac{s}{r}\right)^{10}\right]\cos^4\theta, \tag{1}$$

where U_0 is the hydrogen bond energy at the equilibrium distance, r is the distance between the donor D and the acceptor A, s is their equilibrium distance, and θ is the bond angle between $D-H$ and $H\cdots A$ at equilibrium. For the $O6-H\cdots O3$ hydrogen bond among neighboring cellulose nanofibrils, $s=0.3$nm, $\theta=150^\circ$ (Nishiyama et al., 2002), and $U_0=20$kcal/mol$=1.39\times10^{-19}$J/bond (Parthasarathi et al., 2011). For simplicity, we only consider the variation in the potential energy of hydrogen bonds with respect to the donor–acceptor distance.

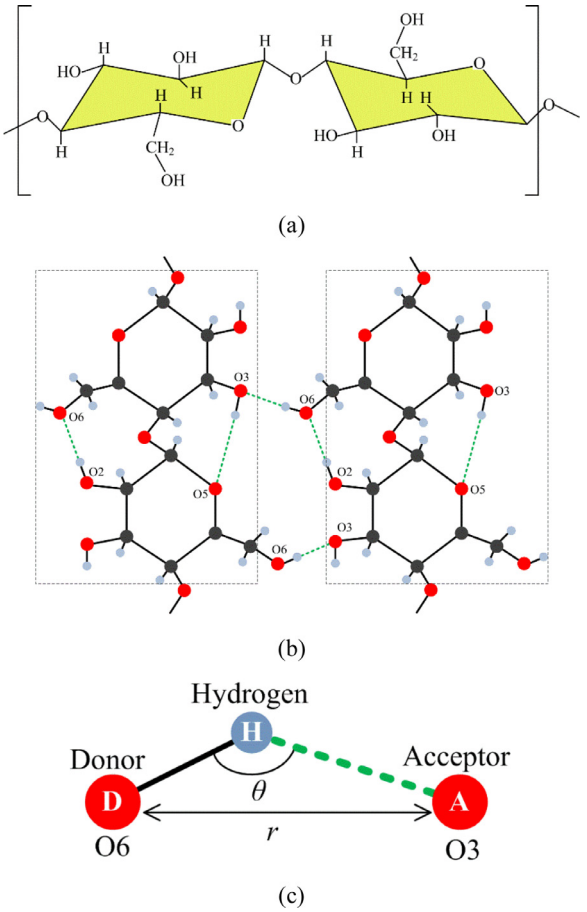

Fig. 1. (a) Molecular structure of a cellulose chain with repeated units. (b) Molecular structure and interfacial hydrogen bonds of neighboring cellulose molecular chains. (c) Hydrogen bond model.

Consider an interface between two cellulose nanofibrils. Assume that the hydrogen bonds at the interface have an average density per unit area, ρ. Then, the cohesive interface energy per unit area can be expressed as

$$\phi = \rho U = \rho U_0 \cos^4\theta \left[5\left(\frac{s}{a}\right)^{12} - 6\left(\frac{s}{a}\right)^{10} \right], \tag{2}$$

where a is the averaged donor–acceptor length of hydrogen bonds at the interface. The equilibrium length a_0 is determined from the minimization of the cohesive energy by using $\partial\phi/\partial a = 0$ at $a_0 = s$.

When the interface opens to a normal displacement u beyond the equilibrium position, the donor–acceptor distance a in the hydrogen bond becomes $a_0 + u$, as shown in Fig. 2(a). Then, the cohesive energy density can be written as

$$\phi = \rho U_0 \cos^4\theta \left[5\left(\frac{s}{a_0+u}\right)^{12} - 6\left(\frac{s}{a_0+u}\right)^{10} \right]. \tag{3}$$

Then the normal cohesive stress σ_{nc} at the interface is

$$\sigma_{\mathrm{nc}} = \frac{\partial\phi}{\partial u} = 60\rho U_0 \cos^4\theta \left[\frac{s^{10}}{(a_0+u)^{11}} - \frac{s^{12}}{(a_0+u)^{13}} \right]. \tag{4}$$

From the derivative of Eq. (4) with respect to u, one can obtain the normal cohesive strength or the maximum cohesive stress

$$\sigma_{\max} = \frac{120}{13}\left(\frac{11}{13}\right)^{\frac{11}{2}} \frac{\rho U_0 \cos^4\theta}{s}, \tag{5}$$

and the corresponding opening displacement at the interface

$$u_0 = \left[\left(\frac{13}{11}\right)^{\frac{1}{2}} - 1 \right] s. \tag{6}$$

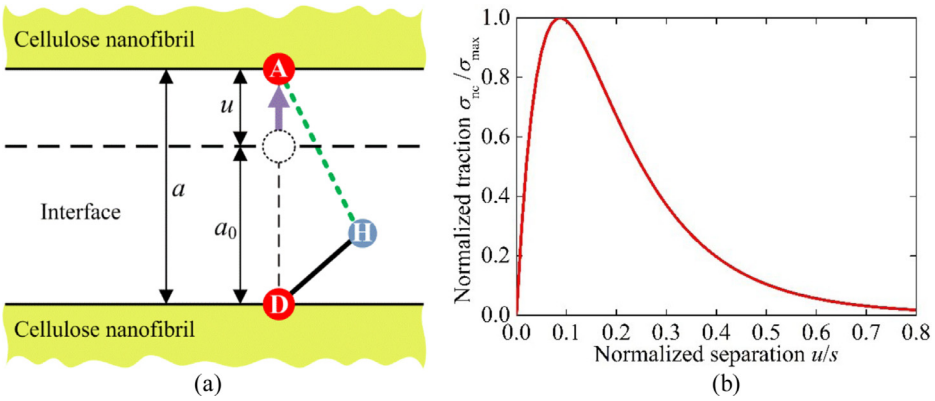

Fig. 2. (a) Schematic of the interfacial interaction due to hydrogen bonds, and (b) the normal cohesive law of the interface.

Besides, the initial slope of the cohesive stress–displacement curve expressed by Eq. (4) is

$$\left.\frac{\mathrm{d}\sigma_{\mathrm{nc}}}{\mathrm{d}u}\right|_{u=0} = \frac{120\rho U_0 \cos^4\theta}{s^2}. \tag{7}$$

The normal cohesive law in Eq. (4) is shown in Fig. 2(b). At the equilibrium position ($u=0$), the interfacial stress is zero. As the interfacial spacing u increases from the equilibrium position, the cohesive traction σ_{nc} first increases rapidly, reaches the cohesive strength $\sigma_{\max}$ at $u=0.09s$, and then decreases gradually.

For a shear displacement v beyond the equilibrium position, the donor–acceptor distance in the hydrogen bond becomes $a=\sqrt{a_0^2+v^2}$, as shown in Fig. 3(a). Then, the cohesive energy density per unit area can be expressed as

$$\phi = \rho U_0 \cos^4\theta \left[\frac{5s^{12}}{(a_0^2+v^2)^6} - \frac{6s^{10}}{(a_0^2+v^2)^5}\right]. \tag{8}$$

Then the shear cohesive stress τ_{sc} at the interface is related to the displacement v by

$$\tau_{\mathrm{sc}} = \frac{\partial\phi}{\partial v} = 60\rho U_0 \cos^4\theta \left[\frac{s^{10}v}{(a_0^2+v^2)^6} - \frac{s^{12}v}{(a_0^2+v^2)^7}\right], \tag{9}$$

as shown in Fig. 3(b). The shear interfacial strength (maximum shear cohesive stress) is obtained from Eq. (9) as

$$\tau_{\max} = \frac{90}{7}\left(\frac{11}{14}\right)^6\left(\frac{3}{11}\right)^{\frac{1}{2}}\frac{\rho U_0\cos^4\theta}{s}, \tag{10}$$

and the corresponding relative slipping displacement is

$$v_0 = \left(\frac{3}{11}\right)^{\frac{1}{2}} s. \tag{11}$$

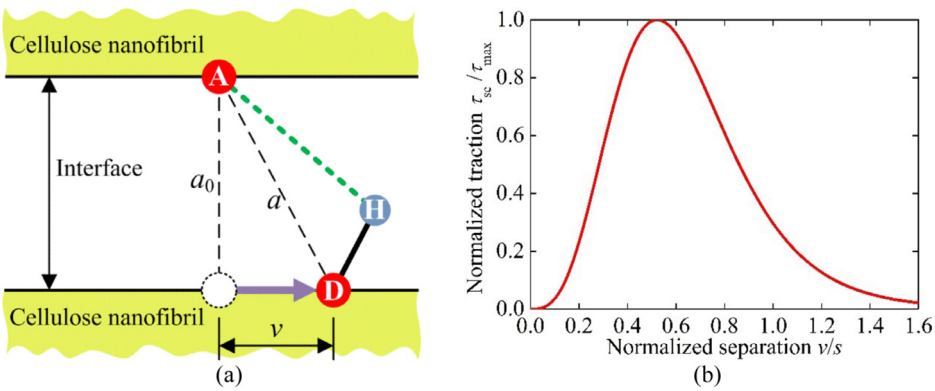

Fig. 3. (a) Schematic of the interfacial shear interaction due to hydrogen bonds, and (b) the shear cohesive law of an interface.

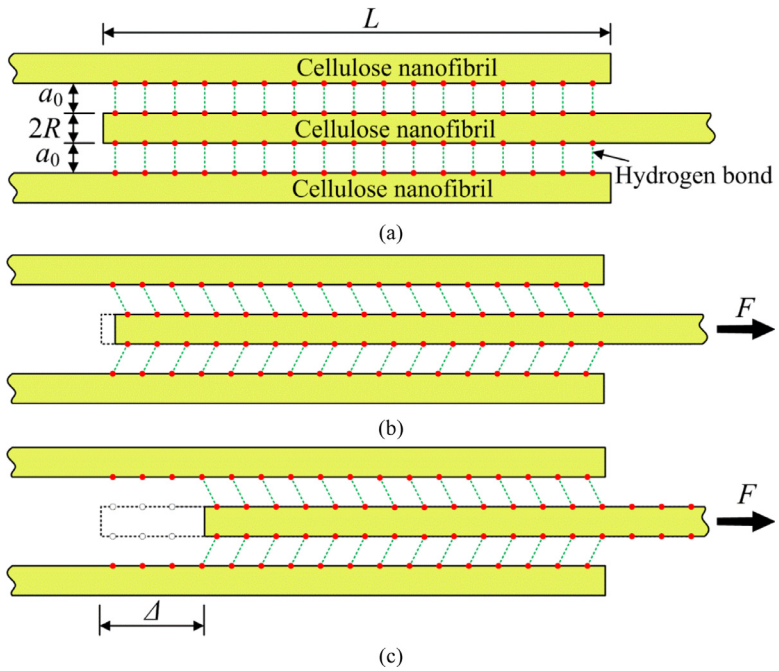

Fig. 4. The pullout process of cellulose nanofibrils. (a) Initial configuration of nanofibrils before loading, (b) interfacial sliding of nanofibrils, and (c) the breaking and reforming of hydrogen bonds.

The initial slope of the shear stress curve is

$$\left.\frac{\mathrm{d}\tau_{sc}}{\mathrm{d}v}\right|_{v=0} = 0. \tag{12}$$

As can be seen from in Figs. 2(b) and 3(b), the cohesive shear stress shows a similar changing tendency to the normal interfacial stress. It can be found that the shear cohesive strength of the interface depends primarily on the density of interfacial hydrogen bonds. From Eq. (10), the cohesive shear strength of the interface is determined as $\tau_{max} = 30\text{MPa}$ when the density of hydrogen bonds is about $\rho = 7.3 \times 10^{16}\text{bonds/m}^2$.

Cellulose nanopaper is composed of a network of cellulose nanofibrils with nanoscale pores. Upon stretching, the initially entangled random cellulose nanofibrils tend to align along the tensile direction (Zhu et al., 2015). In our model, therefore, we assume that due to the high stress concentration at the crack tip, all nanofibrils in the crack-bridging zone are parallel to each other and are normal to the crack surface. Fig. 4 illustrates the pullout process of a cellulose nanofibril, which involves the breakage and reformation of hydrogen bonds at the interface between cellulose nanofibrils (Zhu et al., 2015). Let R denote the radius of cellulose nanofibrils, and L the overlapping length between neighboring nanofibrils (Fig. 4(a)). The entire pullout process of a nanofibril can be divided into the following three stages: (i) In the beginning stage, the center nanofibril undergoes only axial elastic deformation due to the small tensile load. (ii) As the load increases, the nanofibrils slide relatively to each other, corresponding to large relative movements in the cohesive interface with hydrogen bond interactions (Fig. 4(b)). (iii) When the interfacial stress or the sliding displacement reaches a critical value, the hydrogen bonds begin to break and then reform at a new bond site. This process repeats until the center nanofibril is entirely pulled out (Fig. 4(c)). Since the cellulose nanofibrils interact with each other mainly through hydrogen bonds, the sliding stiffness of their interfaces is much weaker than the stiffness of the nanofibrils themselves. In addition, the interfacial shear stress distribution depends on quite a few mechanical and geometric parameters, e.g., the stiffness and dimensions of the nanofibrils and interfaces (Liu et al., 2011). For simplicity, we assume that the cohesive shear stress is uniformly distributed over the interface.

In the pullout process, the tensile force acted on the nanofibril and the cohesive shear stress on the interface satisfies the equilibrium condition:

$$F = 2\pi R(L - \Delta)\tau_c, \tag{13}$$

where Δ is the pullout length of the nanofibril with $0 \le \Delta \le L$. When the cohesive stress on the interface reaches the cohesive shear strength τ_{max}, one has

$$F_c = 2\pi R(L - \Delta)\tau_{max}. \tag{14}$$

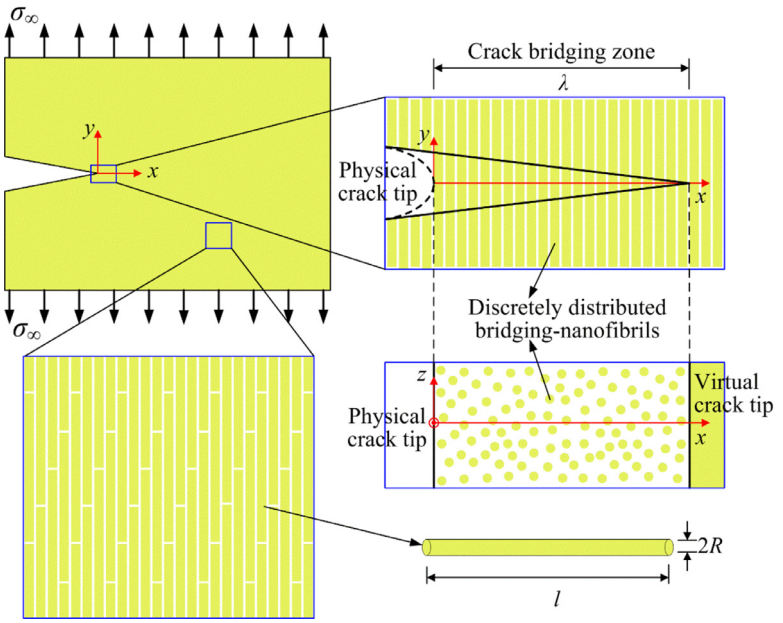

Fig. 5. Schematic of the crack-bridging model for cellulose nanopaper.

For instance, we take the cohesive shear strength $\tau_{max} = 30$MPa, the nanofibril radius $R = 14$nm, the overlapping length $L = 1000$nm, and the nanofibril pullout length $\Delta = 0$. Then it is known from Eq. (14) that the critical tensile force $F_c = 2.64 \times 10^{-6}$N.

3. Crack-bridging model of cellulose nanopaper

Consider a mode-I crack in nanopaper subjected to uniform tension in the far field. During the propagation of the crack, some nanofibrils will be pulled out at the front tip of the crack, leading to the formation of a crack-bridging zone. In this zone, the cellulose nanofibrils repeat the breaking and reforming cycle of hydrogen bonds. In what follows, we will explore the contribution of the crack-bridging mechanism to the fracture toughness of cellulose nanopaper.

A microstructure-based crack-bridging model is proposed to analyze the fracture toughness of cellulose nanopaper, as shown in Fig. 5. The mode-I semi-infinite crack is subjected to a uniform tensile stress σ_∞ along the y-direction in the far field. Let l denote the length of the nanofibrils. The nanopaper, except the crack-bridging zone, is treated as a homogeneous, isotropic elastic solid with elastic modulus E (Henriksson et al., 2008). Assume that the bridging zone length is much smaller than the entire crack length, as observed in experiments (Zhu et al., 2015). The left and right ends of the crack-bridging zone are referred to as the physical crack tip and the virtual crack tip, respectively. The bridging nanofibrils play a shielding role of stresses and eliminate the stress singularity at the crack tip. The fracture toughness can be calculated in terms of the path-independent J-integral or the stress intensity factor K_I^c. In the present study, the modified J-integral defined by Budiansky and Amazigo (1989) is used. The distributed bridging cellulose nanofibrils engender discrete bridging concentrated forces in the crack-bridging zone, which are hard to be individually calculated. For simplicity, therefore the bridging forces are treated by a continuous function of cohesive stress, $\sigma_b(x)$, as shown in Fig. 6(a). The bridging stress $\sigma_b(x)$ depends on the crack opening distance at position x via the cohesive law given in Section 2. When the stress intensity factor in the far field reaches a threshold, the crack will propagate in a steady manner, corresponding to a constant length of the crack-bridging zone. The new bridging nanofibrils form at the front of the crack-bridging zone, whereas the bridged nanofibrils in the rear will be completely pulled out. We will use the stress intensity factor to characterize the fracture toughness of the material.

3.1. Stress intensity factor

When the nanopaper is subjected to a far-field tensile stress σ_∞, the stress intensity factor of the crack in the steady-state of propagation can be written as

$$K_I^\infty = K_I^0 + K_I^b, \tag{15}$$

where K_I^0 is the intrinsic fracture toughness of the nanopaper. The intrinsic fracture toughness of a material reflects the energy dissipation induced by microscopic damage mechanisms that happen around the crack tip during crack propagation (Ritchie, 2011). K_I^∞ denotes the stress intensity factor in the far field, and when the external stress intensity factor reaches

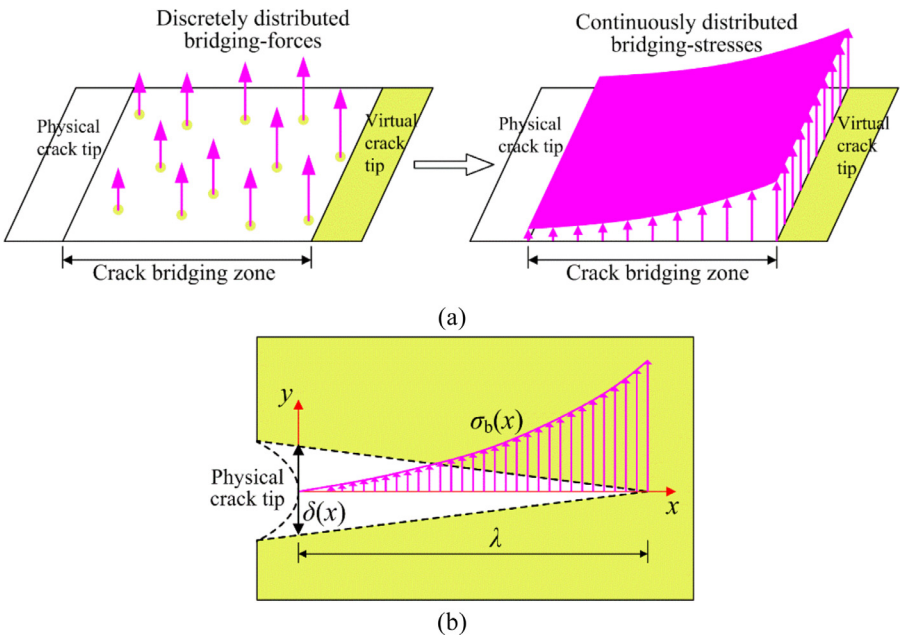

Fig. 6. (a) The homogenization of the bridging force in the crack-bridging zone and (b) the distribution of the bridging stress in the crack-bridging zone.

a critical value, i.e., $K_I^\infty = K_I^c$, the crack will reach the steady-state of propagation, corresponding to the critical fracture toughness of the material. K_I^b is the stress intensity factor induced by the bridging stresses of the cellulose nanofibrils within the crack-bridging zone. It can be calculated by (Budiansky and Amazigo, 1989)

$$K_I^b = \sqrt{\frac{2}{\pi}} \int_0^\lambda \frac{\sigma_b(x)}{\sqrt{\lambda - x}} dx, \tag{16}$$

where λ is the length of the crack-bridging zone, and $\sigma_b(x)$ the cohesive tensile stress in the crack-bridging zone.

In reality, the bridging cellulose nanofibrils are randomly distributed on the crack surfaces within the crack-bridging zone. Let ρ_1 denote the average number of bridging nanofibrils per unit area within the crack-bridging zone. Then, the volume fraction of nanofibrils in the material is

$$V_{bf} = \pi R^2 \rho_1. \tag{17}$$

Denote the pullout length of a nanofiber at coordinate x in the crack-bridging zone as $\delta(x)$; then the corresponding crack opening displacement at this position also equals $\delta(x)$. The maximum pullout length of the bridging nanofibrils is taken as $\frac{l}{2}$, which equals the maximum crack opening displacement at the crack tip. Because the hydrogen bonds keep breaking and reforming during the pullout process, the bridging force induced by a nanofibril at position x can be expressed as

$$F(x) = \pi R \tau_{max}[l - 2\delta(x)]. \tag{18}$$

The bridging stress at position x is

$$\sigma_b(x) = \pi \rho_1 R \tau_{max}[l - 2\delta(x)]. \tag{19}$$

Substituting Eq. (17) into (19) gives

$$\sigma_b(x) = \frac{V_{bf} \tau_{max}[l - 2\delta(x)]}{R}. \tag{20}$$

The distribution of the bridging stress in the crack-bridging zone is shown in Fig. 6(b). Using Eqs. (16) and (20), the stress intensity factor induced by the bridging stresses can be derived as

$$K_I^b = 2\sqrt{\frac{2}{\pi}} \frac{V_{bf} \tau_{max}}{R} \left[\sqrt{\lambda} l - \int_0^\lambda \frac{\delta(x)}{\sqrt{\lambda - x}} dx \right]. \tag{21}$$

It is seen that the contribution of the crack bridge to the toughness, K_I^b, is dependent on the sizes of cellulose nanofibrils, the length of the crack-bridging zone, the cohesive shear strength of intra-nanofibril interface, and the volume fraction of nanofibrils.

3.2. Crack opening displacement

To calculate the length of the crack-bridging zone and the stress distribution in it, one needs to first determine the crack opening displacement $\delta(x)$. For a mode-I semi-infinite crack in an isotropic material, the crack opening displacement can be expressed as (Budiansky and Amazigo, 1989; Shao et al., 2012)

$$\delta(x)=\frac{8K_{\mathrm{I}}^{\infty}\sqrt{\lambda-x}}{\sqrt{2\pi}E}-\frac{4}{\pi E}\int_0^{\lambda}\sigma_{\mathrm{b}}(\zeta)\ln\frac{\sqrt{\lambda-x}+\sqrt{\lambda-\zeta}}{\left|\sqrt{\lambda-x}-\sqrt{\lambda-\zeta}\right|}\mathrm{d}\zeta. \tag{22}$$

The first term in Eq. (22) arises from the far-field stress intensity factor, and the second term is caused by the bridging stresses. Substituting Eqs. (15), (20), and (21) into Eq. (22), the crack opening displacement in the crack-bridging zone is obtained as

$$\begin{aligned}\delta(x)=&\frac{8K_{\mathrm{I}}^{0}\sqrt{\lambda-x}}{\sqrt{2\pi}E}+\frac{4V_{\mathrm{bf}}l\tau_{\max}}{\pi ER}\left[2\sqrt{\lambda(\lambda-x)}-x\ln\frac{\sqrt{\lambda}+\sqrt{\lambda-x}}{\sqrt{\lambda}-\sqrt{\lambda-x}}\right]\\&+\frac{8V_{\mathrm{bf}}\tau_{\max}}{\pi ER}\int_0^{\lambda}\delta(\zeta)\left(\ln\frac{\sqrt{\lambda-x}+\sqrt{\lambda-\zeta}}{\left|\sqrt{\lambda-x}-\sqrt{\lambda-\zeta}\right|}-\frac{2\sqrt{\lambda-x}}{\sqrt{\lambda-\zeta}}\right)\mathrm{d}\zeta\end{aligned}. \tag{23}$$

It is noted that $\delta(x)$ in the crack-bridging zone monotonically decreases with increasing x and satisfies

$$0<\delta(x)\le\frac{l}{2}. \tag{24}$$

A numerical method will be employed to solve $\delta(x)$, with the details given in Appendix A.

3.3. Toughening ratio

After the crack opening displacement and the stress intensity factor in the crack-bridging zone have been solved from Eqs. (21) and (23), we can evaluate the toughening effect of the bridging nanofibrils. To this end, we define the toughening ratio Λ as

$$\Lambda=\frac{K_{\mathrm{I}}^{\mathrm{b}}}{K_{\mathrm{I}}^{0}}=2\sqrt{\frac{2}{\pi}}\frac{V_{\mathrm{bf}}\tau_{\max}}{K_{\mathrm{I}}^{0}R}\left[\sqrt{\lambda}l-\int_0^{\lambda}\frac{\delta(x)}{\sqrt{\lambda-x}}dx\right]. \tag{25}$$

For a crack propagating in a steady state, the length of the crack-bridging zone keeps a constant value, λ_{S}. The corresponding toughening ratio Λ_{S} due to the crack-bridging mechanism is

$$\Lambda_{\mathrm{S}}=\frac{K_{\mathrm{I}}^{\mathrm{bs}}}{K_{\mathrm{I}}^{0}}=2\sqrt{\frac{2}{\pi}}\frac{V_{\mathrm{bf}}\tau_{\max}}{K_{\mathrm{I}}^{0}R}\left[\sqrt{\lambda_{\mathrm{S}}}l-\int_0^{\lambda_{\mathrm{S}}}\frac{\delta(x)}{\sqrt{\lambda_{\mathrm{S}}-x}}dx\right], \tag{26}$$

which is the maximal toughening ratio due to the bridging effect of cellulose nanofibrils.

In addition, the axial stress in a nanofibril should be below its ultimate strength σ_{s}, that is,

$$2\pi R\tau_{\max}\left[\frac{l}{2}-\delta(x)\right]\le\pi R^{2}\sigma_{\mathrm{s}}. \tag{27}$$

At the virtual crack tip, the crack opening displacement is very small and the corresponding pullout length $\delta(x)$ of nanofibrils is close to zero. Then we have

$$l\le\frac{R\sigma_{\mathrm{s}}}{\tau_{\max}}. \tag{28}$$

Table 1
Parameters used in the calculations.

Parameters	Value	References
Elastic modulus E	13.5 GPa	Sehaqui et al. (2011)
Fracture toughness K_{I}^{0}	1 MPa m$^{1/2}$	–
Interfacial shear strength $\tau_{\max}$	30 MPa	–
Nanofibril volume fraction V_{bf}	40%	–
Interfacial thickness l_0	0.3 nm	Nishiyama et al. (2002)
Nanofibril radius R	14 nm	Zhu et al. (2015)
Nanofibril length l	1.5 μm	Moon et al. (2011)
Nanofibril strength σ_{s}	7.5 GPa*	Moon et al. (2011)

* This value is the upper limit of the tensile strength of cellulose nanofibrils.

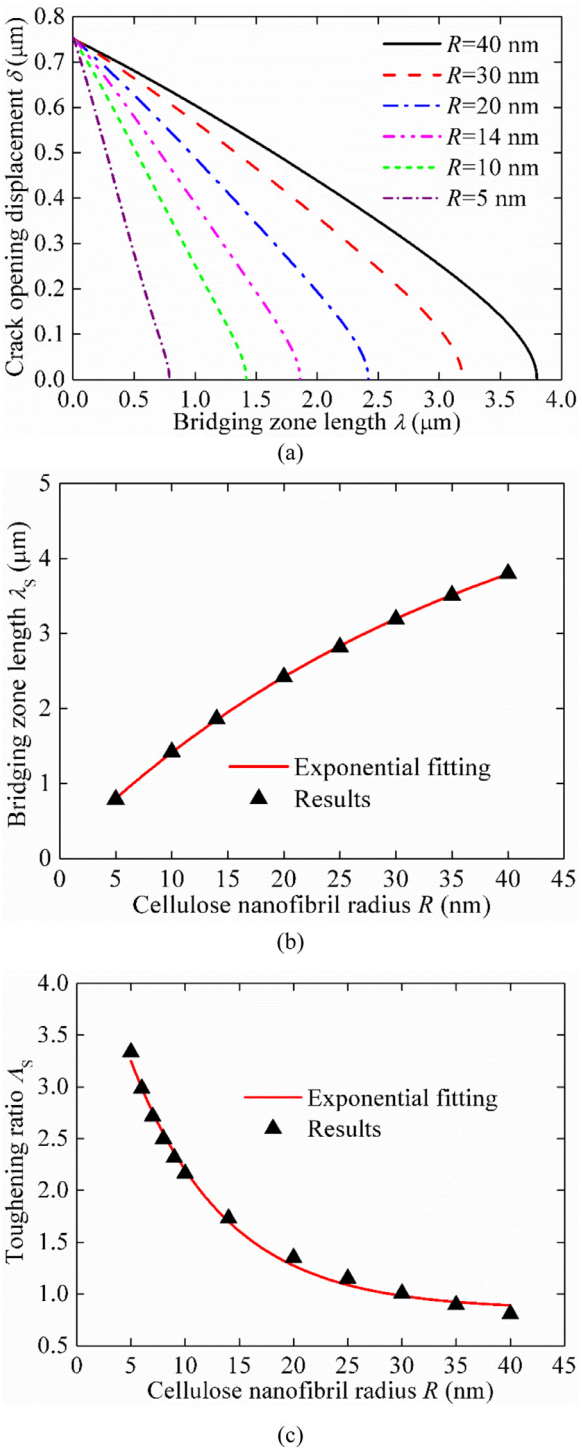

Fig. 7. (a) Crack opening displacement in the crack-bridging zone under steady crack propagation for different cellulose nanofibril radii. Bridging zone length (b) and toughening ratio (c) with respect to the nanofibril radius for steady crack propagation.

Let l_c denote the maximum length of nanofibrils with a given radius R that achieves the strongest toughening effect, and R_c the minimum radius of nanofibrils with a fixed radius l. They are given respectively by

$$l_c = \frac{R\sigma_s}{\tau_{max}}, \quad R_c = \frac{l\tau_{max}}{\sigma_s}. \tag{29}$$

Eqs. (28) and (29) give the optimal sizes of nanofibrils, which help design nanopaper with high fracture toughness.

4. Results and discussions

4.1. Size effects of nanofibrils

Now we examine the effects of nanofibril sizes on the crack-bridging toughening mechanism in cellulose nanopaper. The material parameters used in our calculations are listed in Table 1. The crack opening displacement $\delta(x)$ in the crack-bridging zone is solved from Eq. (23), and the toughening ratio Λ is obtained from Eq. (25). As the applied load increases, more and more nanofibrils are pulled out from the crack surfaces, leading to an extension of the crack-bridging zone and an increase in the crack opening displacement. When the crack opening displacement reaches the maximum value, i.e.$\delta = \frac{l}{2}$, the crack-bridging zone will approach a stable length. Then, the crack enters a steady state of propagation, corresponding to a constant crack-bridging zone length. Therefore, from the condition $\delta = \frac{l}{2}$, we determine the length of the crack-bridging zone λ_S and the toughening ratio Λ_S.

It is hard to make a direct experimental measurement of the intrinsic fracture toughness of cellulose nanopaper. For cellulose nanopaper with the nanofibril radius $R = 5.5$ nm, Zhu et al. (2015) measured the critical strain energy release rate $G_c = 1481.4\ \mathrm{J/m^2}$. Using the relation $K_I^c = \sqrt{G_c E}$, the fracture toughness of nanopaper is determined as $K_I^c = 4.5\ \mathrm{MPa\,m^{1/2}}$. When the nanofibril radius is 14 nm, the strain energy release rate is measured as $G_c = 467.5\ \mathrm{J/m^2}$, corresponding to the fracture toughness $K_I^c = 2.5\ \mathrm{MPa\,m^{1/2}}$. These experiments indicate that the mechanical properties of cellulose nanopaper exhibit significant size effect: the thinner the nanofibrils, the higher the fracture toughness. This size effect can be understood as follows: for a fixed volume fraction of nanofibrils, the decrease in the nanofibril radius will enhance the overall interface area and the number of hydrogen bonds, and thereby yield a significant increase in the fracture toughness of nanopaper. Rich hydroxyl groups along cellulose molecular chains allow for facile formation and reformation of hydrogen bonds at the nanofibril interfaces, leading to an enhanced toughening effect. Zhu et al. (2015) estimated the intrinsic fracture toughness K_I^0 of cellulose nanopaper with the order of 1 $\mathrm{MPa{\cdot}m^{1/2}}$. Therefore, we take $K_I^0 = 1\ \mathrm{MPa{\cdot}m^{1/2}}$ in this study.

For a crack in the steadily propagating state, Fig. 7(a) shows the crack opening displacement $\delta(x)$ in the crack-bridging zone. It can be seen that $\delta(x)$ decreases gradually as the position x approaches the crack tip. For a small nanofibril radius (e.g., $R = 5$ nm), the crack opening displacement decreases relatively rapidly. For steadily propagating crack, Fig. 7(b) and (c) show the bridging zone length and the toughening ratio with respect to the nanofibril radius, respectively. It is seen from Fig. 7(b) that the length of the crack-bridging zone exponentially increases as the nanofibril radius increases, demonstrating that the thinner nanofibrils can render a stronger toughening effect. The steady toughening ratio decreases gradually as the radius of nanofibrils increases. This is because for a given volume fraction of nanofibrils, the smaller the nanofibril radius, the larger the total surface area of the nanofibrils in the crack-bridging zone and, hence, the stronger the bridging toughening effects. This behavior reveals the dependence of the mechanical properties of cellulose nanopaper on the nanofibril radius: the smaller the radius, the greater the fracture toughness. In addition, the lower limit for the nanofibril radius is found from Eq. (28) to be 8 nm since the tensile stress of nanofibrils should be lower than its ultimate strength; otherwise, the nanofibrils will break before being pulled out. The bridging toughening effect of nanofibrils will be reduced when the radius of nanofibrils is smaller than this lower limit. To achieve a remarkable toughening effect, therefore, the radius of nanofibrils should be optimized in an optimal range, which is dictated by both the overall toughening ratio at the macro scale and the tensile strength of the fibrils themselves at the micro scale.

To verify the present model, we compare the theoretical fracture toughness predicted by Eqs. (15) and (26) with the experimental measurements (Zhu et al., 2015), as shown in Fig. 8. It can be observed that the theoretical results agree well with the experimental data. For example, our theoretical model predicts that as the radius of cellulose nanofibrils decreases

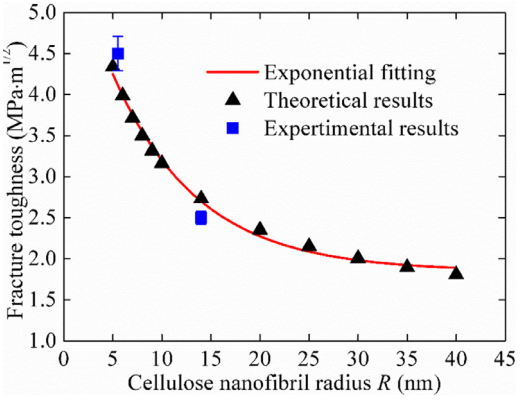

Fig. 8. Comparison of the fracture toughness of cellulose nanopaper predicted by the present model (triangles) and measured in experiments (squares) (Zhu et al., 2015).

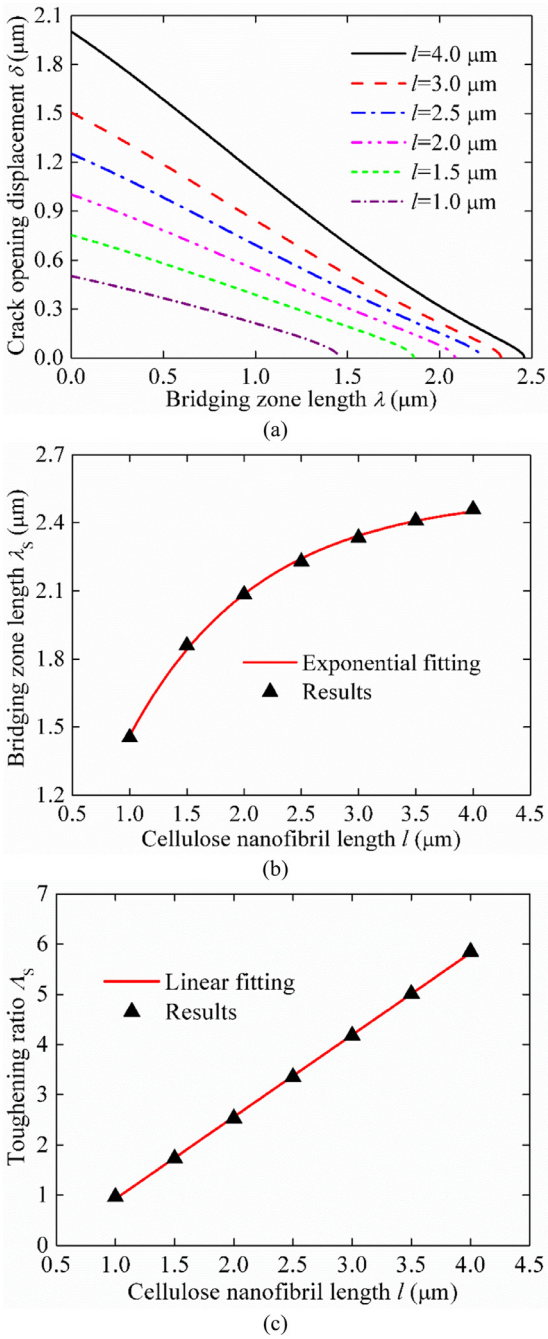

Fig. 9. (a) Crack opening displacement in the crack-bridging zone of a steadily propagating crack under several different cellulose nanofibril lengths. (b) The bridging zone length and (c) the toughening ratio with respect to the nanofibril length.

from $R = 14$ nm to 5 nm, the fracture toughness of cellulose nanopaper varies from $K_I^c = 2.7$ MPa m$^{1/2}$ to 4.3 MPa m$^{1/2}$, and the corresponding experimental values are 2.5 MPa m$^{1/2}$ and 4.5 MPa m$^{1/2}$, respectively.

For a crack propagating in a steady state, Fig. 9(a) shows the crack opening displacement in the crack-bridging zone under a few representative values of cellulose nanofibril lengths. The fracture toughness of nanopaper also exhibits a size dependence on the length of the nanofibrils. Increasing the nanofibril length will lead to a larger bridging zone length and a larger crack opening displacement. Fig. 9(b) and (c) show the effects of the nanofibril length on the bridging zone length and toughening ratio, respectively. Both of them increase with the increase in the cellulose nanofibril length, suggesting that longer nanofibrils will render a longer crack-bridging zone and a higher toughening ratio. However, the length should be

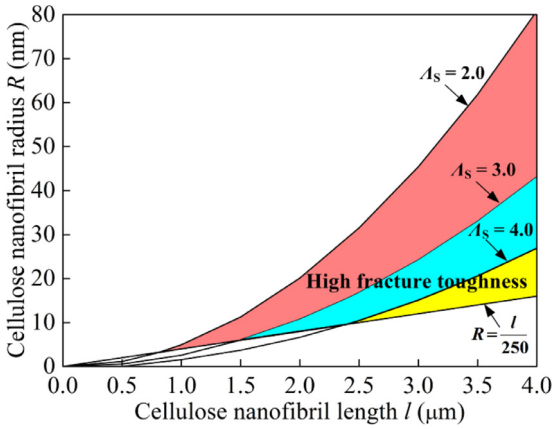

Fig. 10. Contours of the toughening ratio Λ_S with respect to the geometric dimensions of nanofibrils. The red, cyan, and yellow regions give the ranges of nanofibril sizes that yield the toughening ratio $\Lambda_S = 2.0$, 3.0, and 4.0, respectively. (For interpretation of the references to color in this figure legend, the reader is referred to the web version of this article.)

shorter than a certain limit dictated by the tensile strength of the nanofibrils such that they will not be broken before being pulled out. The upper limit of nanofibril length is about 3.5 μm in line with Eq. (28) and Table 1.

The above analysis reveals a strong dependence of the fracture toughness of nanopaper on the radius and length of nanofibrils. To achieve a high toughening ratio, the nanofibril sizes should be in an optimal range. Fig. 10 illustrates the contours of the toughening ratio Λ_S with respect to the geometric dimensions of nanofibrils. It is known from Eq. (28) that the aspect ratio of nanofibrils should be $l/R \leq 250$ when $\tau_{max} = 30$MPa and $\sigma_s = 7.5$GPa. If one wants to design a nanopaper with a toughening ratio Λ_S greater than 2.0, for instance, the nanofibril sizes should be optimized in the shadow region in Fig. 10. Thus, an effective way is here indicated to guide the design of cellulose nanopaper with desired mechanical properties.

4.2. Effects of interfacial strength

In essence, the hydrogen bonds at the interfaces between nanofibrils play a key role in the toughening of cellulose nanopaper. For a crack steadily propagating in nanopaper, Fig. 11(a) shows the crack opening displacement in the crack-bridging zone under a few representative interfacial strengths τ_{max} between cellulose nanofibrils. The change in τ_{max} from 10 MPa to 60 MPa corresponds to an increase in the hydrogen bond density per unit area, ρ, from 2.5×10^{16} bonds/m^2 to 1.5×10^{17} bonds/m^2. The bridging zone length increases gradually with increasing interfacial strength. A higher interfacial strength gives rise to a smaller crack opening displacement. Obviously, the strong interfacial adhesion between cellulose nanofibrils tends to hinder the crack propagation. For a steadily propagating crack, Fig. 11(b) and (c) plot the variations in the bridging zone length and the toughening ratio with respect to the interfacial strength between cellulose nanofibrils. It can be observed that with increasing interfacial strength, the length of the crack-bridging zone decreases exponentially, whereas the steady toughening ratio increases approximately linearly. This result shows that, as expected, improving interfacial strength or hydrogen bond density will result in a higher toughening ratio in nanopaper. In essence, the higher fracture toughness of cellulose nanopaper is attributed to the reformation of hydrogen bonds at the nanofibril interfaces. During the pullout process of a nanofibril, its interfacial stress retains the constant τ_{max} (Fig. 11d). Without the reformation mechanism, the cohesive shear stress would reduce to the interfacial friction traction τ_0 after the breaking of hydrogen bonds (Fig. 11d). In general, τ_0 is much smaller than τ_{max}, and thus the absence of the hydrogen bond reformation mechanism would significantly reduce the fracture toughness, as shown in Fig. 11c. Therefore, the formation feature of hydrogen bonds plays a pivotal role in the mechanical behavior of cellulose nanopaper.

4.3. Effects of elastic modulus

We next examine the effects of the elastic modulus of nanopaper on its fracture toughness. As a porous material, cellulose nanopaper has a relatively high porosity, which significantly influences its macroscopic mechanical properties. As the porosity increases from 19% to 40%, the elastic modulus of nanopaper decreases from 14.7 GPa to 7.4 GPa (Henriksson et al., 2008).

Fig. 12(a) shows the variation in the bridging zone length of a steadily growing crack with respect to the elastic modulus of nanopaper. It is seen that a higher elastic modulus of nanopaper leads to a longer bridging zone, suggesting that the enhanced elastic modulus of nanopaper can better resist the propagation of a crack. The toughening ratio with respect to

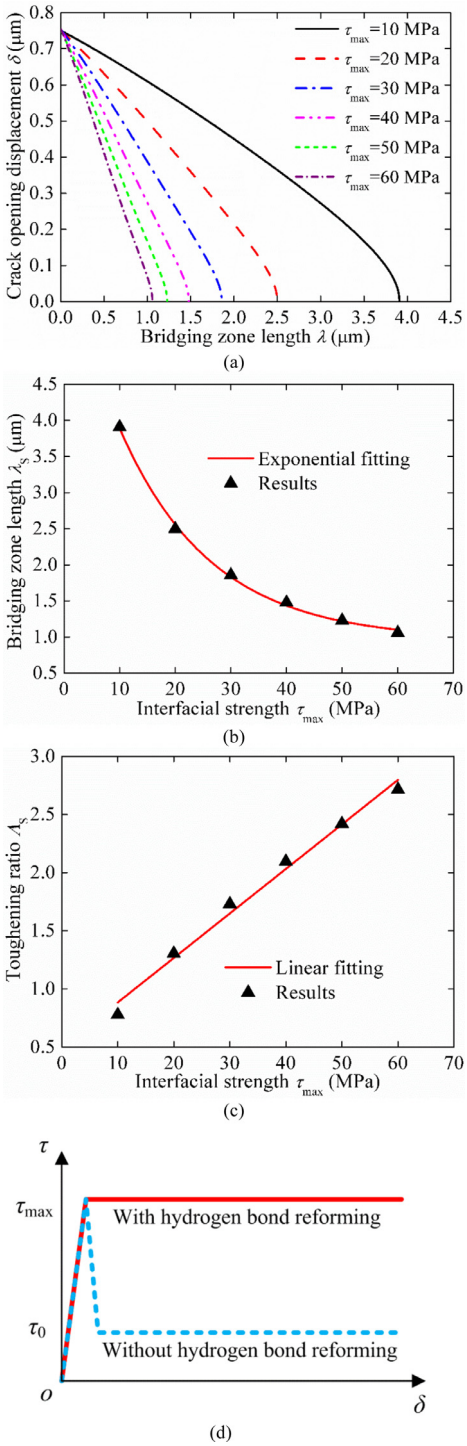

Fig. 11. (a) Crack opening displacement in the crack-bridging zone in a steadily propagating crack under different interfacial strengths between cellulose nanofibrils. (b) The bridging zone length and (c) the toughening ratio with respect to the interfacial strength. (d) Cohesive models for the interfacial shear stress between cellulose nanofibrils with (red solid line) or without (blue dashed line) hydrogen bond reformation mechanism. (For interpretation of the references to color in this figure legend, the reader is referred to the web version of this article.)

the elastic modulus of nanopaper is shown in Fig. 12(b). The steady toughening ratio increases as the elastic modulus of nanopaper increases. Interestingly, this indicates the possible simultaneous achievement of high elastic modulus and high fracture toughness in cellulose nanopaper. Therefore, one should reduce the porosity of cellulose nanopaper in order to improve its mechanical property.

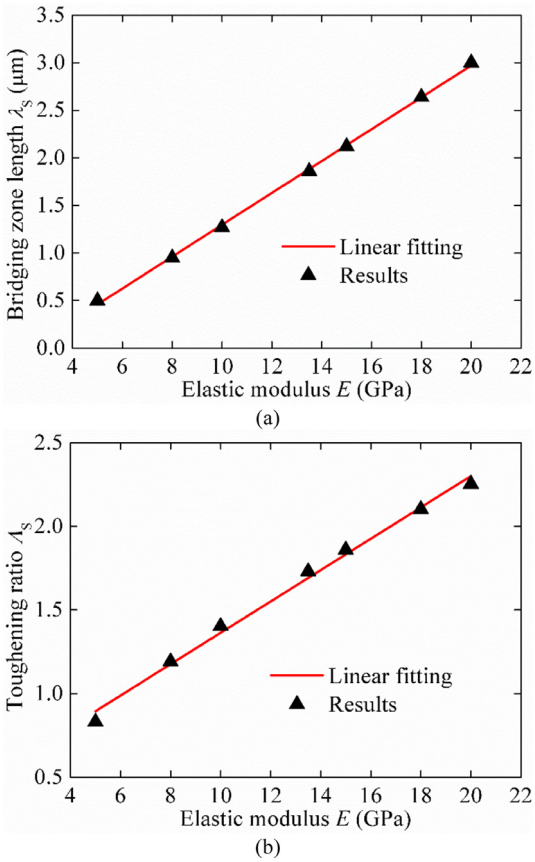

Fig. 12. (a) The bridging zone length and (b) the toughening ratio with respect to the elastic modulus of nanopaper.

4.4. Effects of the volume fraction of bridging nanofibrils

We next analyze the effects of the volume fraction of bridging nanofibrils on the fracture toughness of nanopaper. Fig. 13(a) shows the crack opening displacement in the crack-bridging zone under steady crack propagation for different volume fractions of bridging nanofibrils. It can be found that the crack opening displacement has a smaller value when the volume fraction of bridging nanofibrils is higher. This shows that the enhanced volume fraction of the bridging nanofibril can effectively restrict crack propagation. The bridging zone length and toughening ratio with respect to the volume fraction of bridging nanofibrils for steady crack propagation are shown in Fig. 13(b) and (c). As the volume fraction of bridging nanofibrils increases, the steady bridging zone length decreases, whereas the steady toughening ratio increases. The enhancement of the volume fraction can reduce the length of the crack-bridging zone and improve the bridging toughening ratio and hence, improve the fracture toughness of cellulose nanopaper.

4.5. A unified law for fracture toughness

In the above analysis, we have established the relations between the bridging-toughening ratio and the microstructural parameters of cellulose nanopaper. In this Section, we will perform a dimensional analysis to provide a unified law to correlate the fracture toughness of nanopaper with its microstructure and toughening mechanism.

According to Eqs. (23) and (26), the normalized toughening ratio of cellulose nanopaper should be a function of the following independent parameters

$$\Lambda_S = f(E, \tau_{max}, K_I^0, V_{bf}, l, R), \tag{30}$$

where f is a function as yet to be determined. Among the parameters in Eq. (30), there exist only two independent dimensions, which may be taken as K_I^0 and R. Applying the Pi theorem to Eq. (30) gives

$$\Lambda_S = f\left(\frac{E\sqrt{l}}{K_I^0}, \frac{\tau_{max}\sqrt{l}}{K_I^0}, V_{bf}, \frac{l}{R}\right). \tag{31}$$

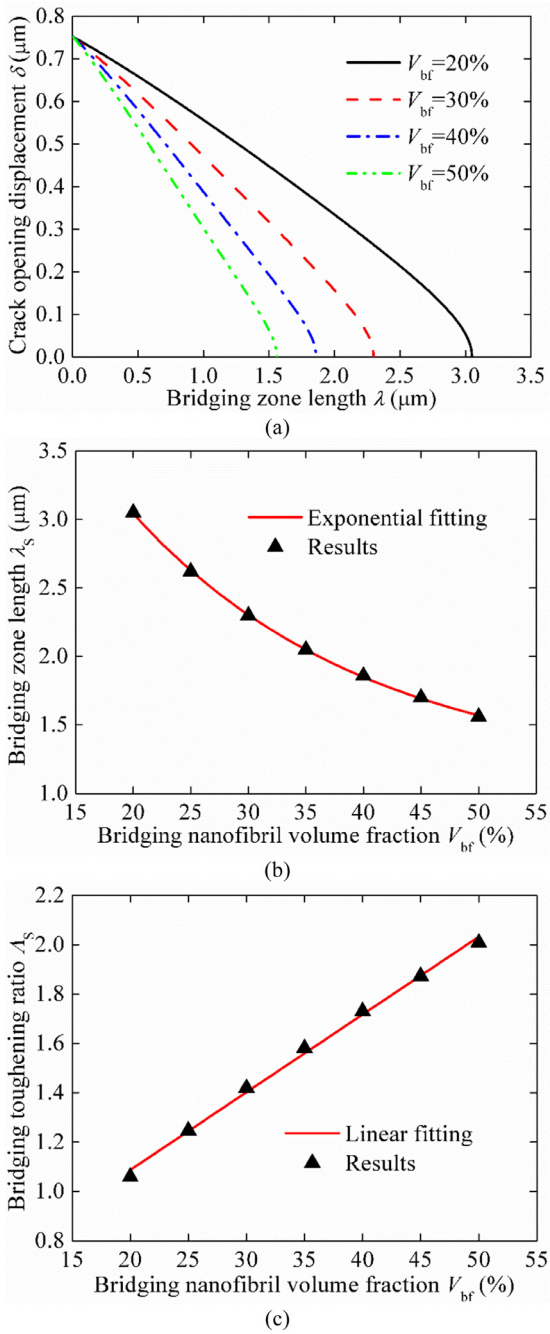

Fig. 13. (a) Crack opening displacement in the crack-bridging zone under steady crack propagation under different volume fractions of bridging nanofibrils. Bridging zone length (b) and toughening ratio (c) with respect to the volume fraction of bridging nanofibrils for steady crack propagation.

Using Eqs. (23), (26), and (31), we obtain the following approximate relation:

$$\Lambda_S = f(\Psi), \tag{32}$$

with $\Psi = \frac{V_{bf} E \tau_{max} l^2}{(K_I^0)^2 R}$.

Fig. 14 shows the variation of the toughening ratio Λ_S with respect to the dimensionless parameter Ψ under different combinations of material parameters, including nanofibril size, interfacial strength, Young's modulus of nanopaper, and volume fraction of bridging nanofibrils. It can be seen that almost all data collapse to the same curve, which can be expressed

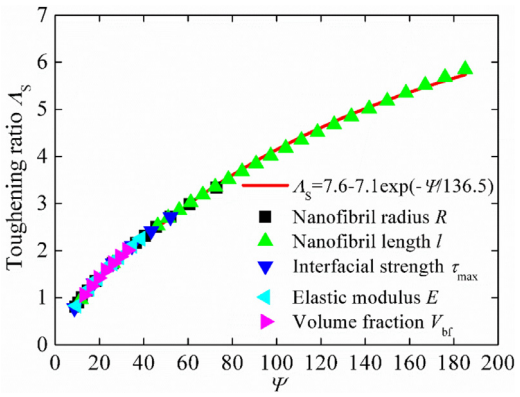

Fig. 14. Variation of the toughening ratio Λ_S with respect to the dimensionless parameter $\Psi = V_{bf}\tau_{max}El^2/(K_I^0)^2R$. The data points here correspond to the following ranges of parameters: $5 \le R \le 40$ nm, $1 \le l \le 4$ μm, $10 \le \tau_{max} \le 60$ MPa, $5 \le E \le 20$ GPa, and $20\% \le V_{bf} \le 50\%$.

via numerical fitting as

$$\Lambda_S = f(\Psi) = 7.6 - 7.1\exp\left(-\frac{\Psi}{136.5}\right). \tag{33}$$

Therefore, according to Eqs. (15), (25), and (33), the fracture toughness of cellulose nanopaper can be written as

$$K_I^c = (\Lambda_S + 1)K_I^0 = \left[8.6 - 7.1\exp\left(-\frac{\Psi}{136.5}\right)\right]K_I^0. \tag{34}$$

Eq. (34) provides a simple theoretical law capturing the relation between the fracture toughness and material parameters of cellulose nanopaper. Given the general applicability of the bottom-up material design strategy obtained from cellulose nanopaper, the above unified law emerging from the present study could be of broad interest in guiding the optimal design of a wide range of engineering materials with superior mechanical properties.

5. Conclusions

In this paper, a multiscale crack-bridging model has been developed to analyze the effects of bridging toughening of nanofibrils on the fracture toughness of cellulose nanopaper. A cohesive law of the interface between cellulose nanofibrils is proposed to link the atomistic level hydrogen bond interaction with the macroscopic interface properties. It is found that both the bridging toughening of nanofibrils and the hydrogen bonds between cellulose nanofibrils serve as significant roles in the toughening mechanisms of cellulose nanopaper. The fracture toughness of cellulose nanopaper has a size dependence on the length and radius of nanofibrils. The thinner and longer nanofibrils can more effectively enhance the crack resistance of cellulose nanopaper. An optimal nanofibril geometry is suggested to achieve a high toughening effect of cellulose nanopaper. Furthermore, a simple unified law emerges from the present theoretical model, which captures the relation between the fracture toughness and material parameters of cellulose nanopaper. Our model not only sheds light on the underlying toughening mechanisms of cellulose nanopaper, but also offers guidelines for the design and optimization of other advanced functional materials.

Acknowledgments

Supports from the National Natural Science Foundation of China (Grant Nos. 11432008, 11672161, and 11542005), China Postdoctoral Science Foundation (Grant No. 2016M590092), the Thousand Young Talents Program of China, and the United States National Science Foundation (Grant No. 1362256) are acknowledged.

Appendix A

The crack opening displacement $\delta(x)$ and the bridging toughening ratio Λ in the crack bridging zone are obtained by numerically solving Eqs. (23) and (25) via the following steps:

(1) We first consider an initial value of the bridging zone length λ; the value of λ gradually increases in the calculation process, which reveals the propagation of the crack-bridging zone. For each λ, the bridging zone ($0 < x < \lambda$) is divided into N subintervals ($N = \frac{\lambda}{\Delta x}$) with sequentially numbered points $0 < x_1 < \cdots < x_i < \cdots < x_N < \lambda$, where $x_i = (i - \frac{1}{2})\Delta x$, and Δx is the length of the subintervals, as shown in Fig. A1. The crack opening displacements at those points are denoted by$\delta(x_i)$.

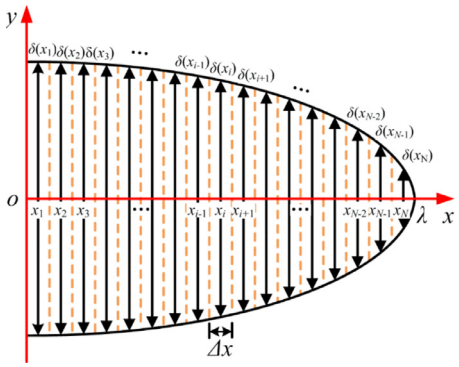

Fig. A1. Schematic of the numerical discretization in the crack-bridging zone.

(2) Applying Eq. (23), the crack opening displacement $\delta(x_i)$ for the each position x_i can be given by

$$\begin{aligned}\delta(x_i) = {} & \frac{8K_I^c\sqrt{\lambda - x_i}}{\sqrt{2\pi}E} + \frac{4V_{bf}l\tau_{max}}{\pi ER}\left[2\sqrt{\lambda(\lambda - x_i)} - x_i \ln\frac{\sqrt{\lambda} + \sqrt{\lambda - x_i}}{\sqrt{\lambda} - \sqrt{\lambda - x_i}}\right] \\ & + \frac{8V_{bf}\tau_{max}\Delta x}{\pi ER}\sum_{\substack{j=1 \\ j\neq i}}^{N}\delta(x_j)\left(\ln\frac{\sqrt{\lambda - x_i} + \sqrt{\lambda - x_j}}{\left|\sqrt{\lambda - x_i} - \sqrt{\lambda - x_j}\right|} - \frac{2\sqrt{\lambda - x_i}}{\sqrt{\lambda - x_j}}\right), \\ & + \frac{8V_{bf}\tau_{max}\Delta x\delta(x_i)}{\pi ER}\left(\ln\frac{\sqrt{\lambda - x_i} + \sqrt{\lambda - x_i - \xi}}{\sqrt{\lambda - x_i} - \sqrt{\lambda - x_i - \xi}} - 2\right)\end{aligned} \tag{A1}$$

where ξ is a small positive constant and $\xi = 10^{-11}$.

(3) From the displacement equation at each position x_i, we can obtain the linear equations with unknowns $\delta(x_i)$, $i = 1, 2, \cdots, N$. By solving the equations, the crack opening displacement for the entire bridging zone can be obtained.

(4) For each λ, we obtain the bridging toughening ratio by the following equation using the crack opening displacement $\delta(x_i)$ at each position x_i:

$$\Lambda = 2\sqrt{\frac{2}{\pi}}\frac{V_{bf}\tau_{max}}{K_I^c R}\left[\sqrt{\lambda}l - \sum_{i=1}^{N}\frac{\Delta x\delta(x_i)}{\sqrt{\lambda - x_i}}\right]. \tag{A2}$$

(5) When the crack opening displacement reaches $\delta(x_N) \geq \frac{l}{2}$, the calculation will stop, indicating that the bridging toughening ratio arrives at a saturated state and the crack propagation enters a steady stage. In addition, we can obtain the bridging zone length λ_S and the toughening ratio Λ_S for the steadily propagating crack.

References

Atalla, R.H., Vanderhart, D.L., 1984. Native cellulose: a composite of two distinct crystalline forms. Science 223 (4633), 283–285.
Bao, G., Song, Y., 1993. Crack bridging models for fiber composites with slip-dependent interfaces. J. Mech. Phys. Solids 41 (9), 1425–1444.
Bao, G., Suo, Z., 1992. Remarks on crack-bridging concepts. Appl. Mech. Rev. 45 (8), 355–366.
Bertoldi, K., Bigoni, D., Drugan, W.J., 2007. A discrete-fibers model for bridged cracks and reinforced elliptical voids. J. Mech. Phys. Solids 55 (5), 1016–1035.
Budiansky, B., Amazigo, J.C., 1989. Toughening by aligned, frictionally constrained fibers. J. Mech. Phys. Solids 37 (1), 93–109.
Chen, X., Beyerlein, I.J., Brinson, L.C., 2011. Bridged crack models for the toughness of composites reinforced with curved nanotubes. J. Mech. Phys. Solids 59 (9), 1938–1952.
Fu, S.Y., Feng, X.Q., Lauke, B., Mai, Y.W., 2008. Effects of particle size, particle/matrix interface adhesion and particle loading on mechanical properties of particulate polymer composites. Compos. Pt. B-Eng. 39 (6), 933–961.
Gao, H., Ji, B., Jäger, I.L., Arzt, E., Fratzl, P., 2003. Materials become insensitive to flaws at nanoscale: lessons from nature. Proc. Natl. Acad. Sci. U. S. A. 100 (10), 5597–5600.
González, I., Alcalà, M., Chinga-Carrasco, G., Vilaseca, F., Boufi, S., Mutje, P., 2014. From paper to nanopaper: evolution of mechanical and physical properties. Cellulose 21 (4), 2599–2609.
Henriksson, M., Berglund, L.A., Isaksson, P., Lindström, T., Nishino, T., 2008. Cellulose nanopaper structures of high toughness. Biomacromolecules 9 (6), 1579–1585.
Hoffman, D.C., Suh, J.Y., Wiest, A., Duan, G., Lind, M.L., Demetriou, M.D., Johnson, W.L., 2008. Designing metallic glass matrix composites with high toughness and tensile ductility. Nature 451 (7182), 1085–1090.
Jang, D., Li, X., Gao, H., Greer, J., 2012. Deformation mechanisms in nano twinned metal nanopillars. Nat. Nanotechnol. 7 (9), 594–601.
Jarvis, M., 2003. Cellulose stacks up. Nature 426 (6967), 611–612.
Ji, B., Gao, H., 2004. Mechanical properties of nanostructure of biological materials. J. Mech. Phys. Solids 52 (9), 1963–1990.
Li, Y.Y., Zhu, H.L., Zhu, S.Z., Wan, J.Y., Vaaland, O., Lacey, S., Fang, Z.Q., Dai, H.Q., Li, T., Hu, L.B., 2015. Hybridizing wood cellulose and graphene oxide toward high-performance fibers. NPG Asia Mater 7, e150.

Lin, Z., Li, V.C., 1997. Crack bridging in fiber reinforced cementitious composites with slip-hardening interfaces. J. Mech. Phys. Solids 45 (5), 763–787.
Liu, G., Ji, B., Hwang, K.C., Khoo, B.C., 2011. Analytical solutions of the displacement and stress fields of the nanocomposite structure of biological materials. Compos. Sci. Technol. 71 (9), 1190–1195.
Liu, Y.F., Masuda, C., Yuuki, R., 1998. Effect of microstructural parameters on the fracture behavior of fiber-reinforced ceramics. Mech. Mater. 29 (2), 111–121.
Mayo, S.L., Olafson, B.D., Goddard III, W.A., 1990. DREIDING: a generic force field for molecular simulations. J. Phys. Chem. 94 (26), 8897–8909.
Meda, G., Steif, P.S., 1994. A detailed analysis of cracks bridged by fibers—I. Limiting cases of short and long cracks. J. Mech. Phys. Solids 42 (8), 1293–1321.
Moon, R.J., Martini, A., Nairn, J., Simonsen, J., Youngblood, J., 2011. Cellulose nanomaterials review: structure, properties and nanocomposites. Chem. Soc. Rev. 40 (7), 3941–3994.
Nishiyama, Y., Langan, P., Chanzy, H., 2002. Crystal structure and hydrogen-bonding system in cellulose Iβ from synchrotron X-ray and neutron fiber diffraction. J. Am. Chem. Soc. 124 (31), 9074–9082.
Parthasarathi, R., Bellesia, G., Chundawat, S.P.S., Dale, B.E., Langan, P., Gnanakaran, S., 2011. Insights into hydrogen bonding and stacking interactions in cellulose. J. Phys. Chem. A 115 (49), 14191–14202.
Qian, X., Ding, S.Y., Nimlos, M.R., Johnson, D.K., Himmel, M.E., 2005. Atomic and electronic structures of molecular crystalline cellulose Iβ: a first-principles investigation. Macromolecules 38 (25), 10580–10589.
Ritchie, R.O., 2011. The conflicts between strength and toughness. Nat. Mater. 10 (11), 817–822.
Rubinstein, A.A., Xu, K., 1992. Micromechanical model of crack growth in fiber-reinforced ceramics. J. Mech. Phys. Solids 40 (1), 105–125.
Sehaqui, H., Allais, M., Zhou, Q., Berglund, L.A., 2011. Wood cellulose biocomposites with fibrous structures at micro- and nanoscale. Compos. Sci. Technol. 71 (3), 382–387.
Shao, Y., Zhao, H.P., Feng, X.Q., Gao, H., 2012. Discontinuous crack-bridging model for fracture toughness analysis of nacre. J. Mech. Phys. Solids 60 (8), 1400–1419.
Shao, Y., Zhao, H.P., Feng, X.Q., 2014a. On flaw tolerance of nacre: a theoretical study. J. R. Soc. Interface 11 (92), 20131016.
Shao, Y., Zhao, H.P., Feng, X.Q., 2014b. Optimal characteristic nanosizes of mineral bridges in mollusk nacre. RSC Adv. 4 (61), 32451–32456.
Sun, C.T., Jin, Z.H., 2006. Modeling of composite fracture using cohesive zone and bridging models. Compos. Sci. Technol. 66 (10), 1297–1302.
Wei, Y.J., Li, Y.Q., Zhu, L.C., Liu, Y., Lei, X.Q., Wang, G., Wu, Y.X., Mi, Z.L., Liu, J.B., Wang, H.T., Gao, H., 2014. Evading the strength–ductility trade-off dilemma in steel through gradient hierarchical nanotwins, Nat. Commun 5, 3580.
Zhu, H., Zhu, S., Jia, Z., Parvinian, S., Li, Y., Vaaland, O., Hu, L.B., Li, T., 2015. Anomalous scaling law of strength and toughness of cellulose nanopaper. Proc. Natl. Acad. Sci. U. S. A. 112 (29), 8971–8976.